CrossMark

He I Vector Magnetic Field Maps of a Sunspot and Its Superpenumbral Fine-Structure

T.A. Schad[1] · M.J. Penn[2] · H. Lin[1] · A. Tritschler[3]

© Springer Science+Business Media Dordrecht 2015

Abstract Advanced inversions of high-resolution spectropolarimetric observations of the He I triplet at 1083 nm are used to generate unique maps of the chromospheric magnetic field vector across a sunspot and its superpenumbral canopy. The observations were acquired by the *Facility Infrared Spectropolarimeter* (FIRS) at the *Dunn Solar Telescope* (DST) on 29 January 2012. Multiple atmospheric models are employed in the inversions because superpenumbral Stokes profiles are dominated by atomic-level polarization, while sunspot profiles are Zeeman-dominated, but also exhibit signatures that might be induced by symmetry-breaking effects of the radiation field incident on the chromospheric material. We derive the equilibrium magnetic structure of a sunspot in the chromosphere and furthermore show that the superpenumbral magnetic field does not appear to be finely structured, unlike the observed intensity structure. This suggests that fibrils are not concentrations of magnetic flux, but are instead distinguished by individualized thermalization. We also directly compare our inverted values with a current-free extrapolation of the chromospheric field. With improved measurements in the future, the average shear angle between the inferred magnetic field and the potential field may offer a means to quantify the non-potentiality of the chromospheric magnetic field to study the onset of explosive solar phenomena.

✉ T.A. Schad
  schad@ifa.hawaii.edu

  M.J. Penn
  mpenn@nso.edu

  H. Lin
  lin@ifa.hawaii.edu

  A. Tritschler
  ali@nso.edu

[1] Institute for Astronomy, University of Hawaii, Pukalani, HI 96768, USA

[2] National Solar Observatory, 950 N. Cherry Avenue, Tucson, AZ 85719, USA

[3] National Solar Observatory, 3665 Discovery Drive, Boulder, CO 80303, USA

1. Introduction

Mapping the upper atmospheric solar magnetic field is essential to understanding the quasi-continual nonthermal heating of the chromosphere/corona. Around sunspots and other field concentrations, the ability of the magnetic field to either suppress or enhance energy transport from the photosphere into the upper atmosphere is being more widely recognized, especially now with the transition region diagnostics of the *Interface Region Imaging Spectrograph* (IRIS) (see, *e.g.*, De Pontieu *et al.*, 2014). This is despite a sincere lack of magnetic field diagnostics in the upper atmosphere. Most observational studies of the influence of the upper atmosphere magnetic field on nonthermal heating have relied on extrapolations of the photospheric field. McIntosh and Judge (2001), in this manner, located 'magnetic shadows' that are thought to be closed field regions of the chromosphere that suppress upward-propagating MHD waves. Complementary, De Pontieu, Erdélyi, and De Moortel (2005) found that photospheric p-mode oscillations may be leaked or channeled into the corona by a reduced effective gravity along inclined magnetic fields, perhaps driving dynamic fine-scaled fibrils and jets around sunspots (Hansteen *et al.*, 2006).

Spectropolarimetric measurements of these fine-scaled chromospheric features are only starting to probe their vector magnetic structure (de la Cruz Rodríguez and Socas-Navarro, 2011; Schad, Penn, and Lin, 2013). Difficulties in the measurement and interpretation of linearly polarized spectral lines formed partially in the chromosphere led early studies to use only *longitudinal* chromospheric magnetograms (Choudhary, Sakurai, and Venkatakrishnan, 2001; Jin, Harvey, and Pietarila, 2013), which give a mixed view of the magnetic environment hosting fibrils. For example, Giovanelli and Jones (1982) argued that fibrils denote local variations in the gas excitation of a more uniform magnetic canopy, while Zhang (1994) suggested that fibrils were regions of concentrated magnetic flux.

Mapping the upper atmospheric magnetic field is also essential to understand the large-scale evolution of active regions and the impulsive release of mass and energy in solar flares and coronal mass ejections (CMEs). Studies of the magnetic structure of active regions have again mostly been limited to the photosphere (see the review by Solanki, 2003), whereas chromospheric magnetic conditions within active regions have been probed with vector magnetometry limited within the strong field regions directly above sunspots and their penumbra (Socas-Navarro, 2005a, 2005b; Orozco Suarez, Lagg, and Solanki, 2005; de la Cruz Rodríguez *et al.*, 2013) or in solar prominences/filaments (Casini *et al.*, 2003; Kuckein, Martínez Pillet, and Centeno, 2012; Orozco Suárez, Asensio Ramos, and Trujillo Bueno, 2014). Yet, mapping the full chromospheric magnetic field above active regions is potentially very useful. We suspect due to the relaxed morphology of the chromosphere's intensity structure that the stresses of the magnetic field dominate over those of the plasma (*i.e.*, a low plasma β). Some evidence is given by Metcalf *et al.* (1995). Extrapolations of the coronal magnetic field should improve with field measurements in such a force-free environment, since current methods with and without preprocessing of the photospheric field to enforce the force-free condition are inconsistent (De Rosa *et al.*, 2009).

Here we demonstrate recent progress in the measurement and interpretation of the He I triplet at 1083 nm, which is formed in the upper chromosphere. We derive unique maps of the chromospheric magnetic field vector extending from within a sunspot umbra out

through its superpenumbra, which demarcates the sunspot outer chromospheric boundary (Bray and Loughhead, 1974). Our work is an extension of that of Schad, Penn, and Lin (2013) (hereafter, Paper I), which determined the full field vector along the spines of individually resolved superpenumbral fibrils. Measurable polarized signals both in linear and circular polarization were found throughout the sunspot and its superpenumbra, ranging from a strong-field Zeeman-dominated regime directly within the sunspot to atomic-level polarization-dominated signatures within the superpenumbral canopy and beyond. Inversions of the Stokes spectra to infer the magnetic field thus require the quantum-level spectropolarimetric modeling of Asensio Ramos, Trujillo Bueno, and Landi Degl'Innocenti (2008). Application of this model distinguishes the maps derived and analyzed here (Section 4) from earlier studies (*cf.*, Lagg *et al.*, 2004; Orozco Suarez, Lagg, and Solanki, 2005; Bloomfield, Lagg, and Solanki, 2007).

2. Observations

We analyze very high sensitivity measurements of the He I triplet polarized spectra at 1083 nm obtained with the *Facility Infrared Spectropolarimeter* (FIRS: Jaeggli, Lin, and Uitenbroek, 2012) during multi-instrument observations at the DST. Paper I described in detail the observational setup used for these observations acquired on 29 January 2012. We describe them here briefly for completeness. The best determination of the chromospheric vector fields comes from a single deep-integration FIRS slit-scan across NOAA Active Region (AR) 11408. The map consists of 200 individual steps of a $77''$ projected-length slit oriented parallel to the solar central meridian (as viewed from Earth) and scanned from solar East to West between 19:16 and 20:50 UTC. Slightly East of the center of the FIRS maps is a single unipolar sunspot, located at N8W35 ($\mu = \cos \Theta = 0.8$; see Figure 1). After full post-facto reduction, the spatial sampling is $0.3'' \times 0.3''$. Long integrations of 7.5 seconds at each slit position resulted in mean noise levels in the polarized Q, U, and V spectra of 4.0×10^{-4}, 3.7×10^{-4}, and 3.0×10^{-4}, in units of continuum intensity (I_C), respectively. Filtered 2D principal component analysis helped remove residual interference fringes (Casini, Judge, and Schad, 2012). These spectra have been corrected for instrumental polarization (estimated error $\lesssim 0.076 \% I_C$), and the wavelength scale has been calibrated in an absolute sense by accounting for Sun–Earth orbital motions, solar rotation, and the solar gravity redshift. Therefore, the reported Doppler velocities correspond to an absolute reference frame fixed to the solar surface (estimated error of ± 250 m sec^{-1}.)

Using standard image-processing techniques, we coaligned the FIRS observations with an intensitygram and longitudinal magnetogram acquired during the FIRS scan by the *Helioseismic and Magnetic Imager* (HMI: Scherrer *et al.*, 2012) on board NASA's *Solar Dynamics Observatory* (SDO). Figure 1, which shows the field of view of all operating DST instruments, is the reference for the continuum structure underlying the FIRS maps discussed in Section 4. A $5.12' \times 5.12'$ portion of the full-disk HMI magnetogram is used below (see Section 4.3) to extrapolate the magnetic field into the upper atmosphere under the current-free approximation.

3. Analysis of the He I Triplet Polarization

A number of mechanisms generate and/or modify polarization in the spectrum of the orthohelium triplet (*i.e.*, He I 1083 nm) (Trujillo Bueno and Asensio Ramos, 2007;

Figure 1 The leading spot of NOAA active region 11408 targeted by the instruments at the *Dunn Solar Telescope* on 29 January 2012 overplotted on and referenced to the SDO/HMI intensitygram (top) and longitudinal magnetogram (bottom) acquired at 20:01:56 UTC. The axes give helioprojective coordinates referenced as seconds of arc away from disk center. He I Stokes profiles gleaned from the sunspot (blue and yellow stars) are shown in Figure 2.
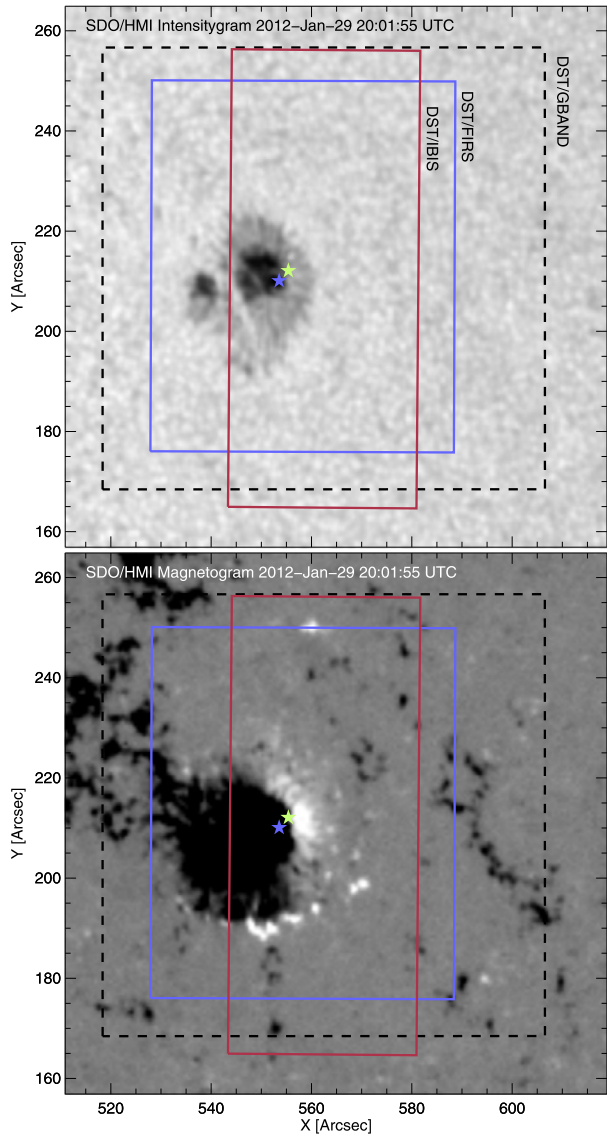
Asensio Ramos, Trujillo Bueno, and Landi Degl'Innocenti, 2008). Paper I identified largely Zeeman dominated Stokes profiles directly above the sunspot umbra and penumbra, while the superpenumbral canopy, wherein 39 resolved fibrils were identified, presented polarized spectra clearly dominated by atomic-level polarization. By atomic-level polarization, we refer to polarization induced by population imbalances of and coherences between the magnetic sublevels of each atomic term in the orthohelium system. Inferring the magnetic field parameters within this regime requires inversions whose forward engine models the emerging Stokes spectra using the full quantum framework. This means solving first the statistical equilibrium equations governing the atomic density matrix for an ensemble of helium atoms subject to an anisotropic radiation field (Landi Degl'Innocenti and Landolfi, 2004).

For the superpenumbra, our inversions employ the Hanle and Zeeman Light diagnostic tool known as HAZEL, which is a forward-modeling and inversion code developed by Asensio Ramos, Trujillo Bueno, and Landi Degl'Innocenti (2008) based on the multiterm calculations of Landi Degl'Innocenti and Landolfi (2004). The radiative transfer equation of the forward model consists of a constant-property slab model including magneto-optical terms and stimulated emission. The slab characteristics, and in turn the modeled and fit Stokes profiles, are quantified by a thermal Doppler broadening, v_{th}, a macroscopic line-of-sight (LOS) velocity, v_{mac}, an optical thickness, $\Delta\tau$, damping parameter, a, magnetic field intensity, B, magnetic field inclination angle, θ_B, magnetic field azimuthal angle, χ_B, and a height, h. A newer parallelized version of the code, known as P-HAZEL, is well-suited for generating maps. Parallelization is essential; each single-point inversion (*i.e.*, each pixel) takes from a minute to a few minutes to complete using a single modern processor and the relatively efficiently optimization scheme implemented by P-HAZEL. For an alternative, promising approach, see the PCA-based optimization scheme used by Casini *et al.* (2003).

3.1. The Influence of Symmetry-Breaking Effects in the Umbra

There is, however, a limitation to using HAZEL to interpret the polarized spectra formed in the strong-field regions of the sunspot umbra and inner penumbra, one that for this particular sunspot led us to adopt a Milne–Eddington model in this region. The limitation stems from its prescription of the pumping radiation field. The degree of atomic-level polarization in the atomic ensemble of helium atoms in the solar atmosphere is controlled in part by the anisotropic properties of the incident radiation field. In its current implementation, P-HAZEL specifies the pumping radiation field incident on a slab of helium atoms at a given height with a classical unpolarized atmosphere, meaning it represents a featureless cylindrically symmetric angle-dependent photospheric continuum flux. This radiation field is fully quantified by two nonzero components of the irreducible spherical radiation field tensor, $J_Q^K(\nu)$, defined as

$$J_Q^K(\nu) = \oint \frac{d\Omega}{4\pi} \sum_{i=0}^{3} T_Q^K(i, \vec{\Omega}) S_i(\nu, \vec{\Omega}), \tag{1}$$

where S_i is the radiation field vector along a ray vector and T_Q^K are irreducial spherical tensors that depend on the reference frame and ray direction (see Section 5.11 of Landi Degl'Innocenti and Landolfi (2004) for further details). Only the $K = 0, 2$ and $Q = 0$ components are necessary to describe the simple classical atmosphere, which greatly reduces the number of statistical equilibrium equations that must be solved in the forward model to calculate the atomic-level polarization. However, in a solar active region, the presence of features such as plages, sunspots, or pores break the cylindrical symmetry. As a consequence, to define the radiation field tensor at each frequency ν associated with a transition in the atomic model requires multispectral knowledge of the localized radiation field. Beyond this complication, incorporating the additional multipole moments of the radiation tensor greatly increases the complexity of the model, leading to an even longer forward-calculation time.

Initially, we attempted to apply the HAZEL model without considering the influence of the additional multiple moments of the radiation field. As a first exercise, we employed HAZEL to invert the polarized spectra observed within the sunspot umbra and penumbra using completely open bounds for the magnetic field direction (*i.e.*, all azimuths from 0 to 360° were allowed). Surprisingly, the majority of the inverted values of the magnetic field azimuthal angles in the superpenumbra represented a diverging sunspot magnetic field
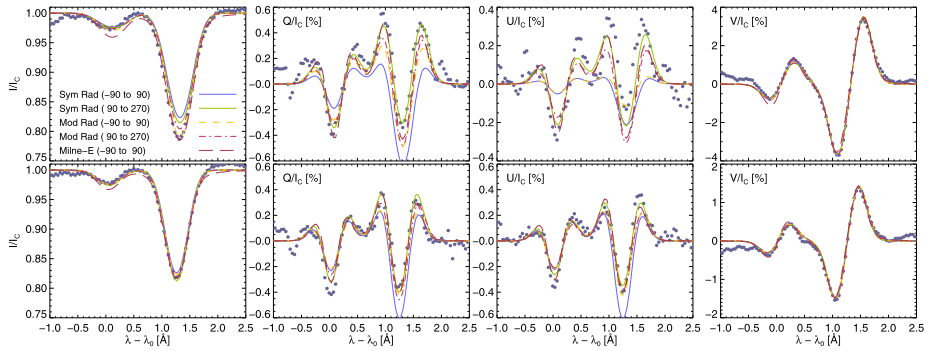
Figure 2 Example umbral (top row) and penumbral (bottom row) He I Stokes spectra extracted from the spatial locations identified by the blue star and yellow star in Figure 1 are given by the data points. HAZEL model fits resulting from constant-property slab models with nominal (solid and triple-dot-dashed lines) and modified (short-dashed and dot-dashed lines) prescribed incident radiation fields are shown alongside a Milne–Eddington model (long dashed line) without atomic level polarization. Goodness-of-fit parameters are given in Table 1.

instead of the expected converging field for a negative polarity sunspot (see Figure 1). This was not a consequence of the optimization algorithm, but the diverging-field solution more adequately fits the Stokes profiles than the converging-field solution.

To better illustrate the challenges posed by the umbral spectra, we inverted two different representative Stokes spectra with seven different forward models. Figure 1 indicates the locations of the observed spectra, which are displayed alongside selected model fits in Figure 2. Models 1 through 6 employ the constant-property slab solution of the radiative transfer equation as in Asensio Ramos, Trujillo Bueno, and Landi Degl'Innocenti (2008), while model 7 uses a Milne–Eddington atmospheric model. For the Milne–Eddington model, we employed the HELIX$^+$ inversion code with its PIKAIA genetic optimization (Lagg *et al.*, 2004; Lagg *et al.*, 2007). Model 7 then includes the Zeeman and Paschen–Back effects on the polarized He I spectra, but no effects of atomic-level polarization. Models 1 and 2 use HAZEL in its nominal mode where the radiation field is cylindrically symmetric. The only difference is that the field solutions are restricted to different ranges of azimuthal angles in a local reference frame orthogonal to the solar surface (No. 1: $-90° < \chi_B < 90°$ and No. 2: $90° < \chi_B < 270°$). Models 3 and 4 are similarly defined by these portions of the magnetic field directional space, but for these models the J_0^0 and J_0^2 components of the radiation field tensor are modified in accordance with the direct calculation given in the Appendix. Models 5 and 6 entirely neglect atomic-level polarization. The resulting magnetic field vectors and reduced χ^2 fit values are reported in Table 1.

The outer umbral spectrum (*i.e.* the blue star) exhibits modification of its linear polarization due to atomic-level polarization, particular in Stokes U, wherein the π lobe of the red triplet component is less strongly polarized than the σ lobes. This effect was similarly witnessed by Lagg *et al.* (2004) and explained by Trujillo Bueno and Asensio Ramos (2007) as signs of atomic level polarization. Alternatively, the inner penumbral spectra shows a clear lack of atomic-level polarization influence. Stokes Q and U for both Stokes spectra are nearly symmetric, suggesting that the $K = 1$ components of the radiation field are negligible. That is, the pumping radiation field does not carry net circular polarization. In addition, the Milne–Eddington model (No. 7) better fits the linear polarization in both cases than the converging field solutions with atomic level polarization (*i.e.*, Nos. 1, 3, 5). The best fit to Q and U in both cases is the diverging field solution for Model 2, as discussed above. In the

Table 1 Comparison of Umbral Inversion Models. Magnetic field vector strength, inclination, and azimuth are specified in the LOS coordinate frame, where inclination is measured relative to the line of sight and the azimuth is referenced as degrees counterclockwise from solar West direction. $\chi^2_{I,Q,U,V}$ refer to the reduced chi-squared goodness-of-fit values for Stokes I, Q, U, and V, respectively.

Model	$B[G]$	$\Theta_B[°]$	$\Phi_B[°]$	χ^2_I	χ^2_Q	χ^2_U	χ^2_V
Outer umbral spectrum – blue star							
1	1463.6	139.8	187.1	2.85	40.2	23.0	12.1
2	1711.7	127.0	15.5	1.67	2.0	5.7	15.6
3	1395.5	131.2	184.7	0.45	13.9	18.8	14.8
4	1592.1	128.6	14.3	0.93	9.1	12.7	13.7
5	1322.9	134.1	184.6	0.37	14.4	19.1	13.8
6	1584.6	129.0	14.3	0.94	10.5	13.6	13.5
7	1363.2	127.1	15.0	0.68	5.4	9.0	44.3
Inner penumbral spectrum – yellow star							
1	1272.8	109.7	201.8	0.41	11.1	11.5	5.5
2	1322.2	107.0	19.9	0.23	2.1	1.9	5.5
3	1269.3	109.9	202.3	0.21	5.4	4.9	4.7
4	1306.4	108.7	19.1	0.16	4.3	4.4	4.6
5	1275.8	109.9	202.3	0.21	4.9	4.3	4.7
6	1292.6	108.3	25.8	0.18	4.8	4.2	4.8
7	1174.2	108.9	21.5	0.50	2.3	2.5	7.0

outer umbral spectrum, the fit for Model 2 is considerably better than most fits, although this field is physically difficult to conceive. We argue, rather, that the non-negligible influence of the radiation symmetry breaking may anomalously lead to the preference of Model 2 although it is unphysical. We show in the Appendix that the $Q \neq 0$ components of the radiation field tensor (especially $Q = \pm 1$) within the sunspot are on the same order of magnitude as the $Q = 2$ component in the nominal quiet classical atmosphere. An alternative explanation could be that a constant-property slab model, as used by HAZEL, may inadequately describe He I formation in the umbra.

Despite great variations in the goodness of fit for the various radiative models (Table 1), the inferred field vector (with 180° ambiguity) remains constant to within ≈ 20 %, which has already been pointed out by Trujillo Bueno and Asensio Ramos (2007). This remains true throughout the sunspot umbra due to the strength of the Zeeman effect. Outside of this region, the atomic-level signatures begin to dominate, but the level of symmetry breaking also greatly decreases.

To quantify the degree of symmetry breaking in the radiation field pumping the He I material, an estimate for the poorly constrained height of the fibrils is necessary. Contribution heights of He I formation range between ≈ 1500 to 2200 km according to nonlocal thermodynamic equilibrium (non-LTE) calculations (Fontenla, Avrett, and Loeser, 1993). Meanwhile, Paper I found a high level of correspondence between He I, Hα, and Ca II fibrils. The numerical models of Leenaarts, Carlsson, and Rouppe van der Voort (2012) argued that Hα fibrils form at heights ranging from 1500 to 2750 km. In accordance with these studies, we selected a nominal height of 1750 km for the height of the He I material in and around the observed sunspot.

Figure 3 Regions of inversion ambiguities across the observed map. The ambiguities result from the combined effects of the saturated Hanle effect ambiguities (*i.e.* the 180° and ±45° Van Vleck LOS azimuth ambiguities) and the 180° azimuthal ambiguity of the transverse Zeeman effect in the Milne–Eddington inversion subregion. The contour outlines the region where no 180° ambiguity exists.
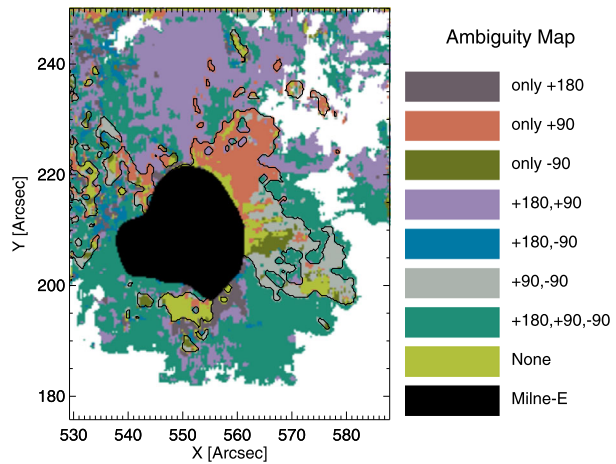
In the Appendix we directly calculate the level of symmetry breaking within the radiation field tensor incident on the He I material. However, simple geometrical considerations supply an estimate for the lateral extent of the sunspot influence. The half-angle of the heliographic extent for the light cone impinging on the raised material is given by

$$\varphi = \frac{\pi}{2} - \gamma \tag{2}$$
$$= \frac{\pi}{2} - \arcsin \frac{R_\odot}{R_\odot + h},$$

where γ is the angle between the solar vertical at the point of the material and the ray tangent to the solar surface. Thus, at a height of 1750 km, φ is 4.06°, meaning that the material located more than φ heliographic degrees away from the symmetry breaking source is unaffected.

3.2. Multimodel Inversions

Inside the sunspot, the inclusion of atomic polarization without extending P-HAZEL to include symmetry-breaking effects may give misleading results. Consequently, we selected the nominal mode of P-HAZEL to invert spectra only outside of the sunspot. Following previous authors (*e.g.* Bloomfield, Lagg, and Solanki, 2007; Orozco Suarez, Lagg, and Solanki, 2005), we used the Milne–Eddington model as implemented in HELIX⁺ to invert the He I triplet spectra where the mean intensity of the pumping radiation, quantified by J_0^0, is reduced by more than 10 % (see black region in Figure 3).

For both models, we used a single magnetized atmospheric component to fit the Stokes spectra. The height of the slab used by P-HAZEL was assumed to be 1750 km above the solar surface, as in Paper I. As shown by Asensio Ramos, Trujillo Bueno, and Landi Degl'Innocenti (2008), errors in the assumed height primarily manifest as errors in the inferred magnetic field inclinations. However, due to the observational noise in these measurements, small differences in the assumed height do not affect the results presented here. A number of pixels exhibit more complex profiles, with multiple, blended velocity components. We identified the pixels whose He I Stokes profiles are better represented by multiple atmosphere components using the Milne–Eddington model (HELIX⁺) to fit one- and two-component model fits to the Stokes I and V spectra alone. We applied the Bayesian information criterion for model selection (see Asensio Ramos *et al.*, 2012) and found that

less than one percent of the profiles in the observed region needs to be fit with multicomponent atmospheres. We did not perform more fits of the these pixels and eliminated them from the remaining analysis. We furthermore ignored all pixels that did not contain a measurable polarization signal (at least 2σ above the noise) in at least one of the Stokes states. Profiles without a measurable Stokes V were still included when the linear polarization was measured. In the superpenumbra, this leads to areas in which the magnetic field intensity is only poorly constrained, as discussed below. The liberal 2σ cutoff was used instead of a more conventional 3σ cutoff to investigate the weak profiles nearest the outer edge of the superpenumbral fibrils. While the inversions of these noisy spectra produce spatially coherent maps of the magnetic field vector, the noisy distribution in the values prevents any conclusive statements about the nature of the outer fibril endpoints.

3.3. Saturated Hanle Effect Ambiguities

To create coherent maps by inverting our observations, we also took into account real physical ambiguities. Just as the transverse Zeeman effect contains an inherent 180° azimuthal ambiguity (in the line-of-sight reference frame), use of atomic-level diagnostics is also affected by ambiguities. Paper I described the possible ambiguities introduced within a classical unpolarized atmosphere for the regime in which the coherences of the atomic ensemble have been destroyed in the magnetic field reference frame. This regime, known as the *saturated Hanle regime*, contains up to eight possible ambiguities for the determination of the magnetic field direction via the linear polarized Stokes vectors (Q and U). With a measurable Stokes V, this number reduces to four, two introduced by the 180° ambiguity, and up to two introduced by the Van Vleck effect.[1] The Van Vleck effect ambiguities are not resolved with Stokes V since the magnetic field strength can be scaled to fit Stokes V in the saturated Hanle regime; Stokes Q and U are unaffected by the field strength up until to a point that the transverse Zeeman effect is significant (Merenda *et al.*, 2006).

The primary Hanle ambiguities do not apply for all field directions (see Merenda *et al.*, 2006) and observational geometries (see Paper I), however. This is a consequence of the preferential axis of the Zeeman effect signal being the line of sight, while that of the atomic-level polarization is the radiation symmetry axis. For example, Stokes V often resolves the 180° Hanle ambiguities for oblique scattering geometries on the solar disk since the other solutions would imply a vastly different orientation with respect to the symmetry axis. For the saturated Hanle regime in a classical atmosphere, the four primary ambiguous solutions (with measurable Stokes V) are not immediately identified by the location of the best-fit solution. According to Landi Degl'Innocenti and Landolfi (2004), these solutions correspond to the linear polarization being oriented either parallel or perpendicular to the projection of the magnetic field vector along the LOS, but the inclination and magnetic field strength of these solutions remain to be determined.

We added another step to the inversion process to find these possible solutions by keeping fixed the thermodynamic parameters of the best-fit solution and fixing the LOS azimuth (Φ_B) of the magnetic field vector in accordance with the saturated Hanle effect ambiguities. That is, we transformed the best-fit P-HAZEL solution into LOS coordinates with $\Phi_{B,\text{best}}$ being the best-fit solution for the azimuthal field direction. The four primary ambiguous solutions are then $\Phi_{B,\text{best}}$, $\Phi_{B,\text{best}} + \pi$, $\Phi_{B,\text{best}} + \pi/2$, and $\Phi_{B,\text{best}} - \pi/2$. Modifying P-HAZEL such that Φ_B is held constant, one iteration of the DIRECT algorithm followed by a fine-tuning iteration of the Levenberg–Marquart algorithm was used to fit two variables: the magnetic field strength B and the inclination in the LOS geometry Θ_B. Once the best-fits

---

[1] See Section 5.8 of Landi Degl'Innocenti and Landolfi (2004) for a discussion of the Van Vleck angle.
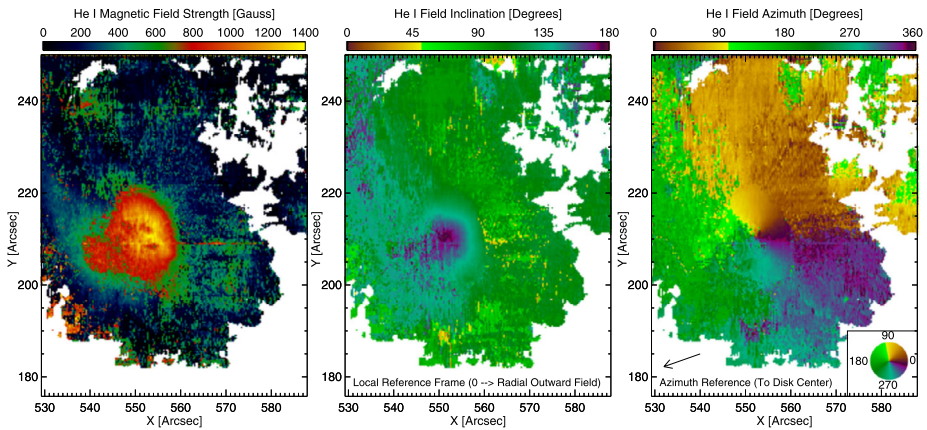
Figure 4 Maps of the magnetic field vector across an active region sunspot and its superpenumbral canopy inferred via analysis of the He I triplet polarized spectra. Ambiguities have been resolved across the region so as to best represent a smooth continuous converging field solution. The field inclination and azimuth are given in the local reference frame. Solar North is up. Solar West is to the right.

are found, they must be verified as ambiguities. We only considered the additional solutions to be ambiguities if the reduced chi-squared values for Stokes Q, U, and V each remained minimally changed ($\Delta\chi^2 < 1$). A map of the regions affected by the various combinations of ambiguities is given in Figure 3. Note that no 180° ambiguity exists for the region northwest of the sunspot. The large Stokes V and the orientation of the fibril fields in this region resolve this ambiguity for that region (see Paper I).

3.4. Ambiguity Resolution

"Disambiguation" refers to the process of *choosing* the ambiguous solution that best represents the solar magnetic field subject to assumptions regarding the physical nature of these fields. At photospheric heights, numerous methods have been applied to real and artificial vector magnetograms with various levels of success (Metcalf *et al.*, 2006). Similarly, maps of the magnetic field in the chromosphere must be disambiguated by choosing the most physically relevant solution. We note that for our observed map, P-HAZEL does not produce a speckled mess of solutions despite the fact that we did not restrict the range of possible magnetic field directions during the inversion process. In most areas, the solution is smooth across the region before disambiguation. This is probably a consequence of the shape of the goodness-of-fit space coupled with the manner in which DIRECT searches for solutions. Furthermore, the ambiguous solutions that we located are rarely strict ambiguities. For the oblique scattering angle, strict ambiguities with identical goodness of fit values may not exist except due to the role of observation noise.

To resolve the He I ambiguities, we developed an interactive routine similar to the AZAM utility developed for the *Advanced Stokes Polarimeter* instrument (Lites *et al.*, 1995). The two primary assumptions made are that the field converges for the negative polarity sunspot and that neighboring pixels give a continuous magnetic field solution. Maps of the disambiguated magnetic field are given in Figure 4; they show a smooth converging field solution with a continuous superpenumbral canopy exhibiting the expected azimuthal change in the field direction around the sunspot. The Milne–Eddington solutions inside the sunspot and the P-HAZEL solutions throughout the canopy show a remarkable spatial continuity at their boundary.

4. Results

4.1. The Chromospheric Magnetic Structure of a Sunspot

In Figure 4, we show the ambiguity-resolved maps of the chromospheric magnetic field vector across the sunspot and the superpenumbra. The magnetic field structure of the superpenumbra exhibits remarkable continuity on the western and northern sides of the sunspot. The third panel of Figure 4 gives the azimuthal angle of the magnetic field in the local frame where the angle is measured relative to the direction of disk center. Thus, the field is converging into the sunspot and wraps around the magnetic field with a nearly radial orientation consistent with the field of fibrils studied by Paper I. The strength of the magnetic field drops from near 1500 Gauss in the sunspot umbra to between 100 and 300 Gauss within the superpenumbral canopy. The superpenumbral canopy is confirmed to be a canopy by the inclination maps, showing values near $90°$, which corresponds to a vector parallel to the solar surface.

We note that the magnetic field strengths on the northwest side of the sunspot in Figure 4 are less noisy than on the southwest side. The 100 to 300 Gauss field strengths place the formation of the He I polarized spectra within the saturated Hanle effect regime, but the transverse Zeeman effect does not give an appreciable signal for these field strengths. As the linear polarization in the saturated regime does not depend on the magnetic field strength, the Stokes V profile determines the field strength. Thus, the field strength is better determined in areas where the structure presents a larger longitudinal component to the observer, explaining why the northwestern side field strengths are more coherent. The fibrillar structure on the southwestern side of the sunspot also exhibits more complex structuring in the *Interferometric Bidimensional Spectropolarimeter* (IBIS) observations of the DST in Ca II 854.2 nm (not shown), which may also lead to a greater level of noise apparent in the magnetic field strengths measured in that region.

The overall structure of the sunspot in the chromosphere is assessed in Figure 5, which shows averages of the field parameters in the azimuthal direction circumscribing the sunspot. Using a cylindrical geometry centered on the nearly circular sunspot (see Paper I), we represent the average structure of the sunspot as a function of sunspot radius, just as in previous studies of the average photospheric structure of sunspots (Beckers and Schröter, 1969; Keppens and Martinez Pillet, 1996). As a result of the error introduced in the magnetic field strength by the weak Stokes V signal discussed above, we studied the average structure only of the northwestern portion of the sunspot in Figure 5. We also compared the average chromospheric magnetic structure with the photospheric magnetic structure inferred from a one-component Milne–Eddington analysis of the Si I spectral line at 1082.7 nm measured by FIRS (see Paper I).

The equilibrium magnetic structure of the sunspot in the chromosphere and photosphere shown in Figure 5 displays significant similarities. In particular, the magnetic field strength decreases as a function of radius, while the inclination of the field decreases (*i.e.*, the field becomes more horizontal). The presence of a light bridge in the umbra (see Figure 1) leads to the relatively flat average behavior of the photospheric magnetic field in the umbra. The chromospheric magnetic field, however, shows a dip in the magnetic field strength within the umbra. In this portion of the umbra, the He I Stokes Q and U spectra do not show clear symmetric profiles and are characterized by an increase in noise. The high-frequency oscillations in the dark umbra probably lead to the disruption of the profiles over the long integration time of the FIRS observations. Still, the approximately 500 Gauss reduction of the field strength in the umbra between the Si I and He I values is consistent with an approximately 0.5 Gauss km^{-1} vertical magnetic field gradient, assuming a 1000 km difference in
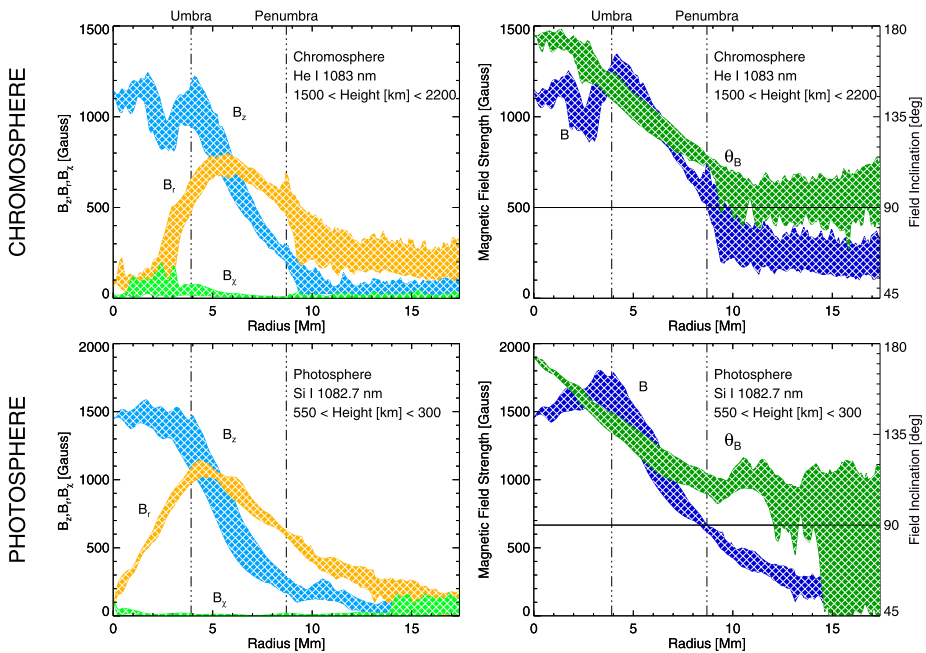
Figure 5 The average magnetic structure of the sunspot in the chromosphere and photosphere, resulting from an analysis of the He I triplet at 1083 nm and the Si I line at 1082.7 nm, respectively. B_z, B_r, and B_χ (left plots) give the strength of the magnetic field components in a cylindrical reference frame centered on the sunspot, while B and θ_B (right plots) show the magnetic field average total strength and inclination angle (relative to the solar vertical).

the formation heights of the two lines in the umbra (Centeno, Collados, and Trujillo Bueno, 2006). It is also clear that the magnetic radius of the sunspot in both the photosphere and chromosphere extends well beyond the outer edge of penumbra viewed in the continuum intensity.

For this observed sunspot, we did not find any significant twist of the magnetic field for either the photospheric or chromospheric observations since the average B_χ component remains negligible (see Figure 5). Thus the torsional forces mainly do not change in an average sense as a function of height. By twist and torsion, we mean the same as Socas-Navarro (2005b), where twist characterizes the non-radial behavior of the field in the cylindrical geometry centered on the sunspot, and torsion refers to the vertical gradient of the azimuthal direction of the field. On a finer scale, clear changes in the azimuthal angle between the photosphere and chromosphere are seen, which is suggestive of complicated torsional forces at work within the sunspot itself. However, since the observations cannot establish the formation height for the He I triplet, projection effects due to the oblique observation angle of these observations can lead to perceived torsional forces that may or may not be real.

Unfortunately, while disk center observations reduce the impact of projection effects, the horizontal nature of the superpenumbral canopy presents a challenge for the He I triplet to infer magnetic field strengths since the linearly polarized signal is very weakly influenced by the magnetic field intensity. Our observations more firmly constrain the field strengths in the superpenumbral canopy that are due to the oblique observation geometry. The superpenumbral canopy fields observed here express a radial gradient smaller than the complementary canopy fields of the upper photosphere measured by Si I (right panels of Figure 5). Outside
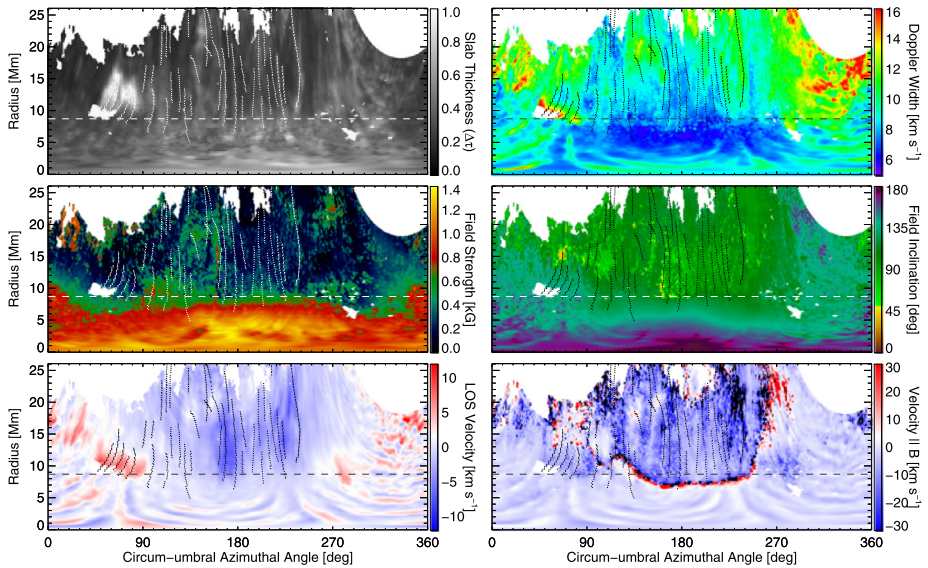
Figure 6 Magnetothermal structuring of the superpenumbral region. The observed FIRS maps are projected onto the cylindrical coordinate system centered on the sunspot, with the dashed line representing the outer penumbral edge. White regions denote areas only poorly fit by the inversions or not measured by the FIRS scan. Dotted lines trace the selected fibrils modeled in Paper I. The panels refer to the quantify indicated by the color bars, with the lower right panel giving the flow velocity magnitude assuming the flow follows the magnetic field lines.

of the penumbral boundary, the photospheric field continues to decrease rapidly, while the chromospheric field becomes nearly constant.

4.2. Fibril and Inter-Fibril Magnetic Structure of the Superpenumbral Canopy

In absence of vector field diagnostics for the regions surrounding sunspots, earlier studies attempted to deduce the magnetic structure of the superpenumbra using longitudinal magnetograms in chromospheric spectral lines. Giovanelli and Jones (1982) argued using Ca II 854.2 nm and Hα magnetograms that the superpenumbral region consisted of a diffuse, but uniform, canopy of magnetic fields extending from the sunspot with a base height of less than 700 km. Noting that the magnetograms did not contain fine-structuring consistent with the fibril structures seen in intensitygrams, the authors concluded that the superpenumbral fibrils do not delineate changes in the field structure, but rather changes in the gas structure and/or excitation. Later work by Zhang (1994) disputed this claim, illustrating fine-scale structures in Hβ magnetograms corresponding to dark filamentary structures extending from a sunspot. This article claimed that superpenumbral fibrils were regions of concentrated magnetic flux. However, interpreting chromospheric filter-based longitudinal magnetograms requires not only considering projection effects, but also fine-scale structuring produced by spatial velocity gradients. With the full vector measurements presented here, we more adequately address the magnetized structure of both the fibrils and the inner fibril plasma.

Figure 6 displays the inferred magneto-thermal structure of the observed active region from the core of the sunspot umbra out to three times its penumbral radius. The images

have been projected onto coordinate axes in the cylindrical reference frame centered on the sunspot. The *x*-axis gives the circumumbral azimuthal angle referenced to the direction of disk center. That is, the region of the image between 90° and 270° corresponds to the half of the sunspot that is farthest from disk center. The inward (blueshifted) Doppler velocities measured in this portion of the sunspot (see lower left panel in Figure 6) are consistent with the inverse Evershed effect (Evershed, 1909). Dotted lines illustrate the paths of the 39 fibrils manually traced in Paper I by inspecting the full spectral data cube. Additional lineated structures not traced in Paper I are apparent in the left top panel that shows the inverted He I slab thickness ($\Delta\tau$). It is important to note that the He I triplet exhibits measurable absorption across the entire observed scan, not just within the fibrils. The fibrils only appear in contrast as regions with greater absorption, most likely due to greater mass densities (see Paper I).

Overall, the magnetic field parameters of Figure 6 (middle panels) support a more uniform magnetic architecture for the superpenumbral region compared to its fine intensity structure, even though the level of noise in the observations does lead to considerable scatter in the returned magnetic field parameters. Still, our measurements indicate that the intensity structuring in the superpenumbra most likely does not result from the concentration of the magnetic field. It is surprising, however, to find that the fibrils are not easily identified in the Doppler-width panel (top right). While there is a gradient towards larger natural line widths with increased distance from the sunspot, the Doppler temperature of the fibrils seems to be only slightly higher than the inner-fibril material.

4.3. Towards Quantifying Nonpotential Energy in the Chromosphere

With a full determination of the magnetic field vector in the chromosphere via the He I triplet, a measure of the nonpotentiality of the region may be obtained by calculating the shear angle between the inferred magnetic field *vector* and the extrapolated current-free field. By using the full measured vector, this method expands that of Jing *et al.* (2011), who performed a similar exercise by calculating the mean shear angle between the azimuthal component of the extrapolated field and the projected azimuthal direction of fine-scaled fibrils observed in pseudo-monochromatic intensitygrams. However, two problems complicate the application of this method. First, we have made an assumption in the inversions regarding the height of the He I material, placing it at 1750 km. The He I observations probably represent not a uniform level of the atmosphere, but rather a corrugated sheet. Until we establish a better constraint for the height, the shear angle may give anomalous values. Second, despite the advanced instrumental capabilities demonstrated here, our measurements still contain a high degree of observational noise relative to the measured signals. Determining the true errors in the inverted quantities remains an area of research. Thus, we here only compare the potential field extrapolation to our inverted quantities instead of quantifying the magnetic shear angle.

We performed a current-free extrapolation of the photospheric magnetic field using a $5.12' \times 5.12'$ subregion of the SDO/HMI longitudinal magnetogram acquired at 20:01:55 UTC (see Figure 1). The subregion was selected so that the upward and downward flux near AR 11408 were approximately balanced. We used the routine called 'FFF' available in the SolarSoft IDL library to calculate the extrapolation based on the equations of Alissandrakis (1981) and Gary (1989). By visual inspection alone, the observed intensity structure of the fibrils exhibit shear with respect to the potential magnetic field lines (see the northwest area of the superpenumbra in Figure 7).

Figure 8 compares the extrapolated and inferred magnetic field vector for each point in our inverted map, at the assumed height of 1750 km. Despite the presence of noise in the
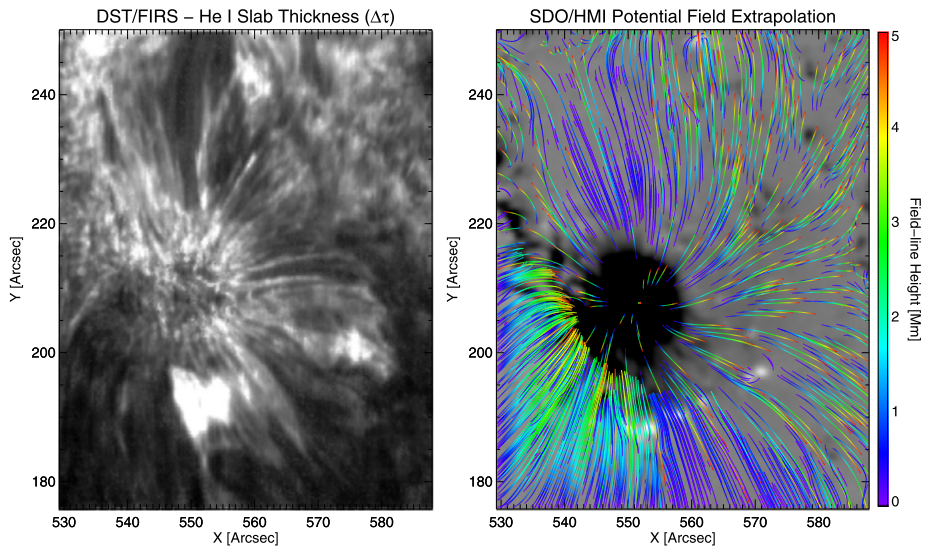
Figure 7 A comparison of the chromosphere fine intensity structuring (left) and the lines of force in a current-free potential field extrapolation of the photospheric magnetic field (right). The left panel gives the inferred slab thickness from P-HAZEL inversions of the observed He I Stokes profiles. Only field lines extending up to 5 Mm above the solar surface are shown on the right. Solar North is up.

inverted quantities, the correlation of the field topology is favorable at all field strengths, with clearly more scatter at lower strengths (blue data points). The inverted magnetic field strengths (assuming a unity filling factor) are generally stronger than the potential field extrapolated from the line-of-sight SDO/HMI measurements. Deviations from the unity line in the azimuth comparison, especially at 50° and 320°, indicate the presence of small amounts of azimuthal shear. However, a few systematic groups of solutions can be identified in the inverted results, which are a product of the high level of noise and the use of the DIRECT optimization algorithm. Still, the majority of the weak-field (*i.e.*, superpenumbral) inclinations cluster at highly inclined horizontal magnetic fields consistent with the potential field extrapolations. However, the degree of scatter is too high to quantify the degree of magnetic nonpotentiality.

5. Discussion and Summary

We have demonstrated the use of the He I triplet at 1083 nm to map and investigate the full vector magnetic field structure of an active region including both a sunspot and its superpenumbral canopy, wherein atomic-level polarization signatures dominate (Schad, Penn, and Lin, 2013). Although the results are promising, one particular challenge faced by our inversions has been the probable influence of a non-symmetric radiation field within and near the outer edges of the sunspot. We neglected this symmetry breaking here, but we argued that the use of a Milne–Eddington model inside the sunspot infers the field parameters with $\approx 20\,\%$ accuracy. With continued work, the symmetry breaking might yet be quite useful, as we suspect the 180° ambiguity of the transverse Zeeman might be overcome by extending the statistical equilibrium equations used by P-HAZEL to include the nonzero K components of the radiation field tensor. This is due to the added constraint placed on the polarization

Figure 8 Comparison of the chromospheric magnetic field intensity (top), inclination (middle), and azimuth (bottom) for the inverted map and a current-free extrapolation of SDO/HMI magnetograms. Inclination and azimuths are given in the local reference frame of the sunspot. Data points are colored according to three ranges in the potential magnetic field intensity (see top panel).
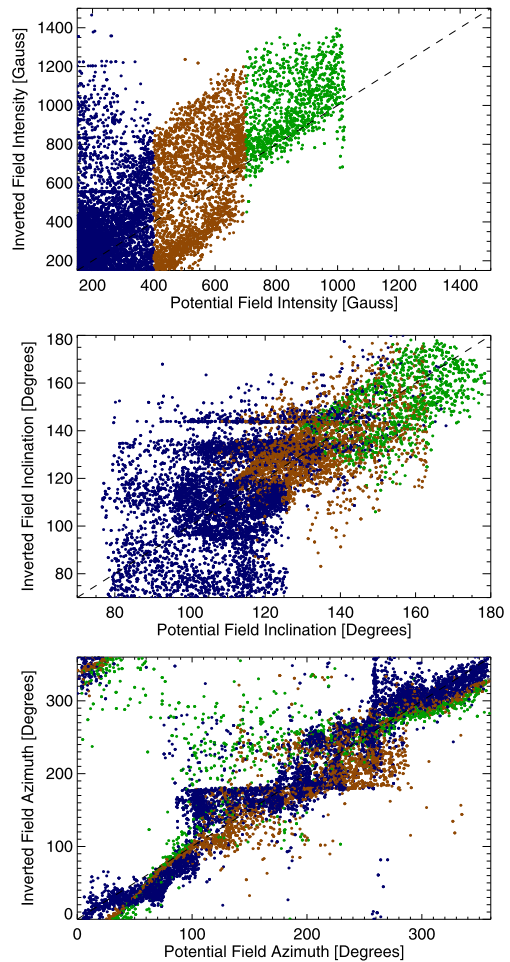
formation by the Hanle effect and the anisotropies of pumping radiation. The greatest challenge for accomplishing this, however, may be the proper determination of the radiation field tensor at the transition frequencies between each major term of the orthohelium atomic model.

Our results favor a fairly homogenous view of the lateral structure of the magnetic field hosting the superpenumbral magnetic canopy, as in Giovanelli and Jones (1982). Evidence is provided by both the spatial continuity in the observed polarization structure and the results of the HAZEL inversions. While the relatively low number of fibrils/filaments observed in low-resolution observations of the superpenumbra can give the impression that the superpenumbra is quite inhomogenous, our results seem intuitive considering the great density of thin fibrils viewed in superpenumbral observations using high-resolution spectral-imagers like IBIS (see Paper I). As Judge (2006) pointed out, the thermal fine-structure of the chromosphere can lead to a more complex notion of the chromosphere than the magnetic field structure supports. In the low-β environment of the upper chromosphere, the average force balance is controlled by the magnetic field, not by the thermal structure. We note, however, that while magnetic canopies may locally exhibit a high degree of homogeneity, the

orientation of the fibrils surrounding magnetic concentrations is influenced by the distribution of the magnetic field in the photosphere (Balasubramaniam, Pevtsov, and Rogers, 2004).

How fibrils become individuated by density and/or thermal perturbations remains an open question. Leenaarts, Carlsson, and Rouppe van der Voort (2012) showed by using advanced 3D non-LTE radiative transfer calculations of Hα that Hα fibrils may be introduced by density enhancements that are aligned with the magnetic field in 3D MHD simulations of the chromosphere. But fibril formation is difficult to constrain observationally, in part due to the difficulty of establishing fibril connectivity with other regions of the atmosphere. Moreover, understanding dynamical activity of fibrils requires connectivity to be established. Thermal stratifications derived using LTE-inversions of the Ca II line at 854.2 nm by Beck, Choudhary, and Rezaei (2014) offer one tentative means to establish connectivity with the photosphere, but magnetic inferences like those presented here are still hindered by observational noise at the outer endpoints of the fibril structures.

On active region scales, we demonstrated that maps of the chromospheric vector magnetic field that include superpenumbral canopy fields can be achieved by inverting the He I triplet. One goal of this study was to provide measurements of the magnetic field at the base of the corona, where the field is more force-free than in the photosphere. This may ease the challenges of extrapolating the coronal magnetic field so that various methods might fall into greater consistency than found by De Rosa *et al.* (2009). However, the observational challenges are still significant, as the level of noise in these already advanced measurements is a hindrance.

In the near future, novel measurement methods (*e.g.*, Schad *et al.*, 2014) for measuring the He I triplet polarization will help to better reap its unique advantages. Higher sensitivity measurements are necessary to exploit the full potential of these He I diagnostics, including its height diagnostic capability. The level of noise in our current He I observations may mask weak fine-structuring of the magnetic field. The height-sensitivity of the He I triplet at 1083 nm may be especially useful in light of the prediction by Leenaarts, Carlsson, and Rouppe van der Voort (2012) that fibrils seen in the Hα spectral line may on average have a greater formation height than the inter-fibril material.

Appendix: The Radiation Field Tensor Near a Sunspot

The pumping radiation field responsible for the development of population imbalances and quantum coherences in the orthohelium atomic system can be fully specified by the irreducible components of the statistical spherical tensor given in Equation (1). In the presence of symmetry-breaking structure, the radiation field tensor can be determined by numerically integrating the radiation field given by the observed continuum structure of the region. Our observations give the normalized continuum intensity near 1083 nm. Thus, the absolute photometric intensity across the region can be inferred from the observations using the known limb-darkening law at 1083 nm. Then, by transforming first to the local frame of reference of a given point in the atmosphere at height, h, we find the nonzero radiation field
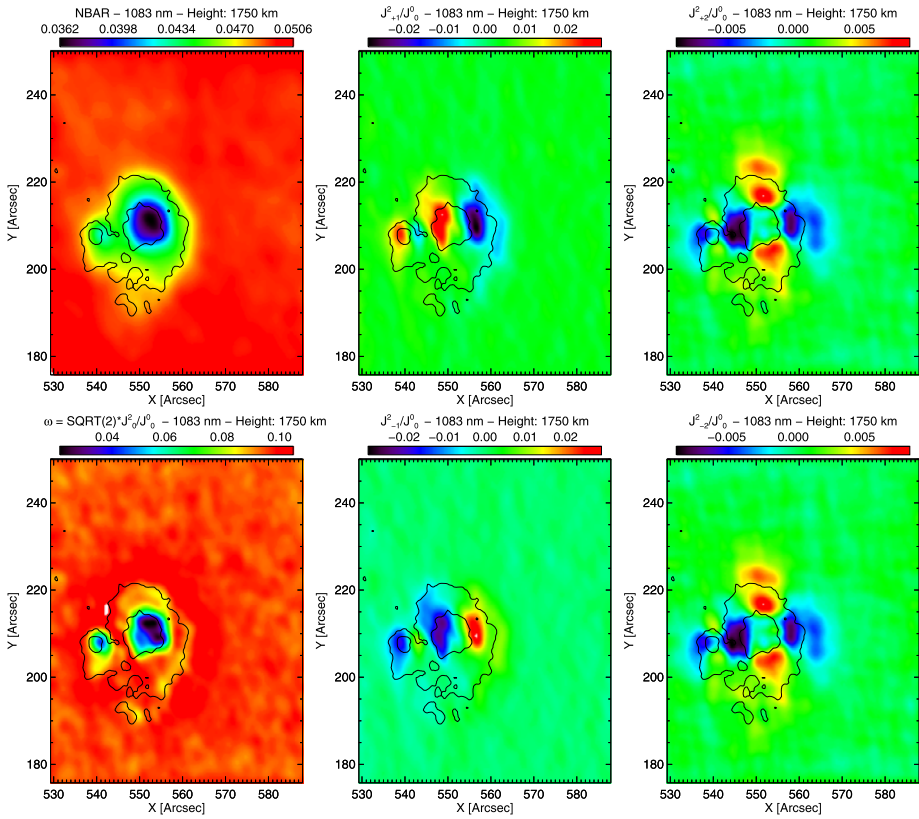
Figure 9 Multipole moments of the local radiation field tensor for a slab of material located at a height of 1750 km above the solar surface. Only the real part of $Q = \pm 1, 2$ components is displayed. NBAR represents the zero moment, where NBAR is defined as $\bar{n} = (c^2/2h\nu^3)J_0^0$.

tensor components by applying the following expressions assuming the radiation field is unpolarized,

$$J_0^0(\nu) = \oint \frac{d\Omega}{4\pi} I(\nu, \vec{\Omega}),$$ (3)

$$J_0^2(\nu) = \frac{1}{2\sqrt{2}} \oint \frac{d\Omega}{4\pi} (3\cos^2\theta - 1) I(\nu, \vec{\Omega}),$$ (4)

$$J_{\pm 1}^2(\nu) = \mp \frac{\sqrt{3}}{2} \oint \frac{d\Omega}{4\pi} \sin\theta\cos\theta e^{\pm i\chi} I(\nu, \vec{\Omega}),$$ (5)

$$J_{\pm 2}^2(\nu) = \frac{\sqrt{3}}{4} \oint \frac{d\Omega}{4\pi} \sin^2\theta e^{\pm 2i\chi} I(\nu, \vec{\Omega}),$$ (6)

which are the expansion of Equation (1) for $i = 0$. We follow the geometry used in Section 12.3 of Landi Degl'Innocenti and Landolfi (2004). Iterated Gaussian quadrature bivariate integration is used to numerically integrate these equations. The results are illustrated in Figure 9 for a height of $h = 1750$ km. Only the real portion of the $Q = \pm 1, 2$ components is shown.

The symmetry breaking is most pronounced within the sunspot. Contours of the inner and outer penumbral edges show the sunspot's photospheric extent (Figure 9). The mean

intensity structure given by $\bar{n}$ (see Figure 9) is slightly offset from the photospheric structure due to the observational geometry of the region, and the assumed height of the helium slab. The weak ring structure in the map of ω best illustrates the extent of the radiative symmetry breaking in the superpenumbra. The half-angle of the heliographic extent of the light cone at this height is 4.06°, whereas the entire heliographic extent of the observed region is $4.44° \times 5^{\cdot}$. The effect of the $Q = \pm1$ components is minimal beyond the sunspot edge, whereas the $Q = \pm2$ components show pronounced changes within the inner superpenumbral region. However, the magnitude of these components is an order of magnitude below that of the J_0^2 component. Figure 9, of course, only shows the radiation field tensor at the frequency of one transition within the orthohelium atomic system. As a result of the variation of the Planck function, we might expect the magnitude of the $Q \neq 0$ components to increase at shorter wavelengths where the sunspot contrast is enhanced; but overall, the effect of this symmetry breaking around the penumbral edge is expected to be an order of magnitude below the J_0^2 component, which itself induces very weak polarization signatures of $\lesssim 0.1$ % of the incoming intensity.

References

Alissandrakis, C.E.: 1981, *Astron. Astrophys.* **100**, 197. ADS.

Asensio Ramos, A., Trujillo Bueno, J., Landi Degl'Innocenti, E.: 2008, *Astrophys. J.* **683**, 542. DOI. ADS.

Asensio Ramos, A., Manso Sainz, R., Martínez González, M.J., Viticchié, B., Orozco Suárez, D., Socas-Navarro, H.: 2012, *Astrophys. J.* **748**, 83. DOI. ADS.

Balasubramaniam, K.S., Pevtsov, A., Rogers, J.: 2004, *Astrophys. J.* **608**, 1148. DOI. ADS.

Beck, C., Choudhary, D.P., Rezaei, R.: 2014, *Astrophys. J.* **788**, 183. DOI. ADS.

Beckers, J.M., Schröter, E.H.: 1969, *Solar Phys.* **10**, 384. DOI. ADS.

Bloomfield, D.S., Lagg, A., Solanki, S.K.: 2007, *Astrophys. J.* **671**, 1005. DOI. ADS.

Bray, R.J., Loughhead, R.E.: 1974, *The Solar Chromosphere*, Chapman & Hall, London. ADS.

Casini, R., López Ariste, A., Tomczyk, S., Lites, B.W.: 2003, *Astrophys. J. Lett.* **598**, L67. DOI. ADS.

Casini, R., Judge, P.G., Schad, T.A.: 2012, *Astrophys. J.* **756**, 194. DOI. ADS.

Centeno, R., Collados, M., Trujillo Bueno, J.: 2006, *Astrophys. J.* **640**, 1153. DOI. ADS.

Choudhary, D.P., Sakurai, T., Venkatakrishnan, P.: 2001, *Astrophys. J.* **560**, 439. DOI. ADS.

de la Cruz Rodríguez, J., Socas-Navarro, H.: 2011, *Astron. Astrophys.* **527**, L8. DOI. ADS.

de la Cruz Rodríguez, J., Rouppe van der Voort, L., Socas-Navarro, H., van Noort, M.: 2013, *Astron. Astrophys.* **556**, A115. DOI. ADS.

De Pontieu, B., Erdélyi, R., De Moortel, I.: 2005, *Astrophys. J. Lett.* **624**, L61. DOI. ADS.

De Pontieu, B., Rouppe van der Voort, L., McIntosh, S.W., Pereira, T.M.D., Carlsson, M., Hansteen, V., Skogsrud, H., Lemen, J., Title, A., Boerner, P., Hurlburt, N., Tarbell, T.D., Wuelser, J.P., De Luca, E.E., Golub, L., McKillop, S., Reeves, K., Saar, S., Testa, P., Tian, H., Kankelborg, C., Jaeggli, S., Kleint, L., Martinez-Sykora, J.: 2014, *Science* **346**, D315. DOI. ADS.

De Rosa, M.L., Schrijver, C.J., Barnes, G., Leka, K.D., Lites, B.W., Aschwanden, M.J., Amari, T., Canou, A., McTiernan, J.M., Régnier, S., Thalmann, J.K., Valori, G., Wheatland, M.S., Wiegelmann, T., Cheung, M.C.M., Conlon, P.A., Fuhrmann, M., Inhester, B., Tadesse, T.: 2009, *Astrophys. J.* **696**, 1780. DOI. ADS.

Evershed, J.: 1909, *Observatory* **32**, 291. ADS.

Fontenla, J.M., Avrett, E.H., Loeser, R.: 1993, *Astrophys. J.* **406**, 319. DOI. ADS.

Gary, G.A.: 1989, *Astrophys. J. Suppl.* **69**, 323. DOI. ADS.

Giovanelli, R.G., Jones, H.P.: 1982, *Solar Phys.* **79**, 267. DOI. ADS.

Hansteen, V.H., De Pontieu, B., Rouppe van der Voort, L., van Noort, M., Carlsson, M.: 2006, *Astrophys. J. Lett.* **647**, L73. DOI. ADS.

Jaeggli, S.A., Lin, H., Uitenbroek, H.: 2012, *Astrophys. J.* **745**, 133. DOI. ADS.

Jin, C.L., Harvey, J.W., Pietarila, A.: 2013, *Astrophys. J.* **765**, 79. DOI. ADS.

Jing, J., Yuan, Y., Reardon, K., Wiegelmann, T., Xu, Y., Wang, H.: 2011, *Astrophys. J.* **739**, 67. DOI. ADS.

Judge, P.: 2006, In: Leibacher, J., Stein, R.F., Uitenbroek, H. (eds.) *Solar MHD Theory and Observations: A High Spatial Resolution Perspective*, *Astron. Soc. Pacific* **CS-354**, San Francisco, 259. ADS.

Keppens, R., Martinez Pillet, V.: 1996, *Astron. Astrophys.* **316**, 229. ADS.

Kuckein, C., Martínez Pillet, V., Centeno, R.: 2012, *Astron. Astrophys.* **539**, A131. DOI. ADS.

Lagg, A., Woch, J., Krupp, N., Solanki, S.K.: 2004, *Astron. Astrophys.* **414**, 1109. DOI. ADS.

Lagg, A., Woch, J., Solanki, S.K., Krupp, N.: 2007, *Astron. Astrophys.* **462**, 1147. DOI. ADS.

Landi Degl'Innocenti, E., Landolfi, M. (eds.): 2004, *Polarization in Spectral Lines*, *Astrophys. Space Sci. Lib.* **307**. ADS.

Leenaarts, J., Carlsson, M., Rouppe van der Voort, L.: 2012, *Astrophys. J.* **749**, 136. DOI. ADS.

Lites, B.W., Low, B.C., Martinez Pillet, V., Seagraves, P., Skumanich, A., Frank, Z.A., Shine, R.A., Tsuneta, S.: 1995, *Astrophys. J.* **446**, 877. DOI. ADS.

McIntosh, S.W., Judge, P.G.: 2001, *Astrophys. J.* **561**, 420. DOI. ADS.

Merenda, L., Trujillo Bueno, J., Landi Degl'Innocenti, E., Collados, M.: 2006, *Astrophys. J.* **642**, 554. DOI. ADS.

Metcalf, T.R., Jiao, L., McClymont, A.N., Canfield, R.C., Uitenbroek, H.: 1995, *Astrophys. J.* **439**, 474. DOI. ADS.

Metcalf, T.R., Leka, K.D., Barnes, G., Lites, B.W., Georgoulis, M.K., Pevtsov, A.A., Balasubramaniam, K.S., Gary, G.A., Jing, J., Li, J., Liu, Y., Wang, H.N., Abramenko, V., Yurchyshyn, V., Moon, Y.-J.: 2006, *Solar Phys.* **237**, 267. DOI. ADS.

Orozco Suarez, D., Lagg, A., Solanki, S.K.: 2005, In: Innes, D.E., Lagg, A., Solanki, S.A. (eds.) *Chromospheric and Coronal Magnetic Fields*, *ESA* **SP-596**, ESA, Noordwijk, 59. ADS.

Orozco Suárez, D., Asensio Ramos, A., Trujillo Bueno, J.: 2014, *Astron. Astrophys.* **566**, A46. DOI. ADS.

Schad, T.A., Penn, M.J., Lin, H.: 2013, *Astrophys. J.* **768**, 111. DOI. ADS.

Schad, T., Lin, H., Ichimoto, K., Katsukawa, Y.: 2014, In: Ramsay, S.K., McLean, I.S., Takami, H. (eds.) *Ground-based and Airborne Instrumentation V*, *Proc. SPIE* **9147**, 6. DOI. ADS.

Scherrer, P.H., Schou, J., Bush, R.I., Kosovichev, A.G., Bogart, R.S., Hoeksema, J.T., Liu, Y., Duvall, T.L., Zhao, J., Title, A.M., Schrijver, C.J., Tarbell, T.D., Tomczyk, S.: 2012, *Solar Phys.* **275**, 207. DOI. ADS.

Socas-Navarro, H.: 2005a, *Astrophys. J. Lett.* **633**, L57. DOI. ADS.

Socas-Navarro, H.: 2005b, *Astrophys. J. Lett.* **631**, L167. DOI. ADS.

Solanki, S.K.: 2003, *Astron. Astrophys. Rev.* **11**, 153. DOI. ADS.

Trujillo Bueno, J., Asensio Ramos, A.: 2007, *Astrophys. J.* **655**, 642. DOI. ADS.

Zhang, H.: 1994, *Solar Phys.* **154**, 207. DOI. ADS.